Available online at www.sciencedirect.com
SCIENCE DIRECT®
Coordination Chemistry Reviews 248 (2004) 1491–1499
COORDINATION CHEMISTRY REVIEWS
www.elsevier.com/locate/ccr

Review

Correlation of morphology and device performance in inorganic–organic TiO_2–polythiophene hybrid solid-state solar cells

Luke B. Roberson [a], Mark A. Poggi [a], Janusz Kowalik [a,*], Greg P. Smestad [b,1], Lawrence A. Bottomley [a], Laren M. Tolbert [a]

[a] *School of Chemistry and Biochemistry, Georgia Institute of Technology, Atlanta, GA 30332, USA*
[b] *Sol Ideas Technology Development, P.O. Box 5279, San Jose, CA 95150-5729, USA*

Received 2 November 2003; accepted 10 February 2004
Available online 17 April 2004

Contents

Abstract

Flat solid-state polymer photovoltaic (PV) cells were constructed using undoped poly(3-undecyl-2,2′-bithiophene) (P3UBT) and flat titanium dioxide (TiO_2) films prepared using a sol–gel technique. Layers and interfaces were studied using AFM, SEM, EDX, XPS, and optical microscopy to determine the impact of the interfacial boundary morphology on the PV device performance. Friction mapping and surface roughness measurements of the fluorinated tin oxide (SnO_2:F) conductive glass, TiO_2, and P3UBT surfaces show a distinct difference in surface contours enabling a better understanding of light absorption as well as charge separation and injection by the polymer. It was found that each working layer in the photovoltaic device exhibited a planarizing effect, where each successive film was slightly smoother than the underlying layers. TiO_2 films greater than 70 nm in thickness fractured during sintering and all films failed following sintering times exceeding 1 h at 450 °C. Fracture of the TiO_2 film resulted in exposure of the underlying SnO_2:F glass and short-circuited solar cells. The film thickness varied with viscosity of the sol–gel and could be controlled by the synthesis conditions and age of sol–gel used. Additionally, the hydrophilic TiO_2 surfaces readily absorbed water when exposed to ambient conditions thereby altering the interfacial boundary and degrading PV cell performance. Spin-coated P3UBT deposited at high concentrations and low spin speeds was found to deposit a layer a few nanometers thick containing polymer aggregates between 5 and 30 μm in diameter, which resulted in a solar cell with $J_{sc} = 2\ \mu A/cm^2$ and $V_{oc} = 0.2$ V. The optimized spin- and cast-coated P3UBT layers were used with the best TiO_2 films to create flat solid-state photovoltaic inorganic–organic hybrid cells with $J_{sc} = 55\ \mu A/cm^2$ and $V_{oc} = 0.5$–0.7 V. Films with fewer defects and aggregates yielded better PV device performance.

Keywords: Atomic force microscopy (AFM); Friction mapping; Solar cell; Organic–inorganic hybrid; Photovoltaic; TiO_2

* Corresponding author. Tel.: +1-404-894-4078; fax: +1-404-894-7452.
E-mail addresses: janusz.kowalik@chemistry.gatech.edu (J. Kowalik), smestad@solideas.com (G.P. Smestad).
[1] Co-corresponding author.

0010-8545/$ – see front matter © 2004 Elsevier B.V. All rights reserved.
doi:10.1016/j.ccr.2004.02.013

1. Introduction

The electronics generation has created an ever-increasing demand for energy to fuel the new technologies of the 21st century; therefore, the need for new forms of energy conversion to meet this demand is imperative. Traditional fossil fuel energy sources are finite and their release of waste products into the atmosphere is detrimental to the earth's global environment. As an alternative, methods for efficient conversion of wind, hydroelectric, and solar energy into electrical energy are being explored to solve the world's energy dilemma [1]. Solar power is attractive due to the abundance and consistency of sunlight; therefore, inorganic semiconductors and, more recently, organic-based solar cells have been explored to develop an inexpensive yet efficient method for the conversion of solar light into energy. The genesis of standard silicon solar cells development occurred in the 1950s when Chapin et al. reported the first crystalline solar cell with a power conversion efficiency of 6% [2]. To date, modern solar energy conversion is still only between 15 and 20% efficient, yet they remain expensive both in development and commercialization [3,4].

Atomic force microscopy (AFM) is an important analytical tool that has been used in the characterization of the interfaces in solar cell devices [5–7]. It has been used in the characterization of TiO_2 films commonly used in organic–inorganic hybrid solar cells [8–10]. Recent reports presented a correlation between the thickness of the TiO_2 film and its surface roughness [11,12]. Zaharescu et al. presented results suggesting a relationship between the processing temperature and surface topography of TiO_2 films [13].

Organic materials are being investigated to determine the effectiveness of charge carrier mobilities and charge injection mechanisms in polymer-based solar cells [14], light emitting diodes (LEDs) [15], and field effect transistors (FETs) [16,17]. One approach to low cost organic PV devices is based on the sensitization of a high bandgap material, such as TiO_2 with organic dyes such as *cis*-$(SCN)_2$ bis(2,2′-bipyridyl-4,4′-dicarboxylate)ruthenium(II) [18]. This dye coordinates to the TiO_2 surface at the interface between the two materials and forms a new light absorbing composite with unique photophysical properties. This dye-sensitized solar cell (DSSC) approach was pioneered by Michael Grätzel and co-workers at the Swiss Federal Institute of Technology in Lausanne. It has yielded PV devices with efficiencies that are comparable to commercially viable inorganic thin film solar cells (AM1.5, $J_{sc} = 16\,mA/cm^2$ and in sunlight to electrical energy conversion efficiency of 7–10%, as well as quantum efficiencies of 80–90% from 400 to 700 nm) [18]. Only a monolayer of the dye is utilized as the light absorber on the high surface area semiconductor support. The high surface area multiplies light absorption while allowing for efficient charge collection at the dye–TiO_2 interface. Photon-induced charge carrier production and transport are carried out by two different types of materials, the dye, and electron and hole conductors, respectively.

The inorganic layer plays two important roles in an inorganic–organic hybrid DSSC. The main purpose of the inorganic semiconductor is to accept the electron from the excited state of the dye, formed upon absorption of light, while at the same time, preventing recombination of the newly formed electron–hole pair. The better optimized the bandgap of the inorganic material is, vis-à-vis organic sensitizer, the more efficient the charge separation and PV device performance. An astute approach to controlling the interfacial charge recombination dynamics has been recently reported by Durrant and co-workers [19]. The inorganic layer also acts as a blocking layer by preventing direct, physical contact, and thus avoiding an electrical short between the SnO_2:F electrode and a hole conductor. Inorganic oxides with appropriate bandgaps are typically chosen as inorganic layers in DSSC applications. We have chosen TiO_2 because of its optical and physical properties and our familiarity with its synthesis.

The originally developed DSSC PV device utilizes an iodine-iodide redox mediator dissolved in acetonitrile to transport holes [20]. Although the efficiency of light conversion was spectacular, one limitation of this liquid electrolyte-based DSSC approach is that the use of low viscosity, highly volatile solvents impedes commercialization. A number of solutions have been proposed to solve this problem. One includes replacement of the liquid junction with a gel electrolyte [21–23]. Our previous reports have shown that the liquid electrolyte in the DSSC can be replaced with suitable substituted polythiophenes [1,24,25] using a flat interface in order to carry out basic studies without the complicating effects of pore filling and light absorption by hole conductors. In these initial studies, it was found that one needs to completely understand and control the interface between the organic and inorganic portions of the PV cell in order to facilitate events occurring at that interface. As part of our continuing interest in the development of organic–inorganic hybrid solar cells, we initiated an investigation of the relationship between surface morphology and solar cell performance [1]. In this report, we critically examine the morphology of each layer in a hybrid solar cell, relating the surface coverage to solar cell functionality.

2. Experimental

2.1. Sol–gel TiO_2 electrode preparation

Nanoporous TiO_2 films were prepared using the sol–gel methods previously reported by several groups [24,26,27]. A 500 μl aliquot of titanium(IV) isopropoxide ($Ti(^iPrO)_4$) was added to a solution containing 10 ml of dry ethanol, 250 μl of nanopure water (purified using a NanoPure water filtration system), and 2–5 drops of nitric acid so that the pH was between 1 and 2. The reaction was carried

out using Schlenk techniques under an argon atmosphere. Ti(^{i}PrO)$_4$ was added dropwise at a slow rate. The solution was stirred vigorously for 24–48 h before applying to the substrate. Fluorine-doped conductive tin oxide (SnO_2:F or CTO: 1.0 cm × 1.0 cm and 1.0 cm × 1.5 cm, sheet resistance ∼15 Ω/cm^2) glass plates purchased from Hartford Glass were used as electrode substrates. The conductive glass substrates were cleaned in triplicate using deionized water and either acetone or isopropanol. An approximate 2 mm section of glass was covered using Kapton tape to create an electrode contact (hereinafter referred to as the contact tab) and care was taken to prevent underflow of sol–gel during deposition. The sol–gel solution was spin-coated onto the substrates at spinning speeds of 17, 33, 50, 83 rps using a Laurel Technologies WS-400A-6NPP-LITE spin coater. Samples were dried under ambient conditions for several minutes. They were then placed in a Lindberg furnace and sintered at 450 °C from 30 to 60 min. The temperature of the furnace was ramped to 450 °C at 25 °C/min and, following sintering at the desired time period, ramped down to 120 °C at 50 °C/min with an air flow rate of 10 ml/min. Upon cooling to 120 °C, TiO_2 samples were immediately removed from the furnace and placed into dry chloroform to prevent them from interacting with moisture.

2.2. Polymer synthesis and deposition

P3UBT was synthesized using Sugimoto-type oxidation methods previously reported [28,29]. Sintered TiO_2 samples to be coated with P3UBT were initially placed in a protecting solution containing 0.04, 0.40, and 4.0 mg/ml P3UBT in chloroform; however, due to aggregate formation upon drying, this procedure was abandoned and dried chloroform was used instead. The samples were then placed onto the spin coater where two subsequent 100 μl applications of warm 0.4 mg/ml or 4.0 mg/ml P3UBT in chloroform were spun at 17, 33, or 50 rps. It was necessary to filter and heat the polymer solution prior to deposition to promote a uniform polymer film and reduce aggregate formation. Polymer solutions were filtered using a 0.2 μm PTFE Aerodisc syringe filter. The polymer films were dried upon completion of spinning. Chloroform (Fisher) was used to clean residual polymer on the contact tab, edges, and underside of the conductive glass and were then stored in a desiccator until they were analyzed or made into PV cells.

2.3. PV cell construction

The edges of the remaining polymer layer were masked with Kapton tape to create a well 0.20 cm^2 or 0.25 cm^2 in area. Two to six drops of hot 4.0 mg/ml solution of P3UBT in chloroform were deposited into the well and dried slowly to create a thick, uniform film resistant enough to prevent the carbon particles from punching through the polythiophene layer. A hole-punch was used to remove a circular area in a piece of electrical tape. The tape was then positioned over the top of the polymer as a contact mask. Carbon powder (Merck 4206) dried at 110 °C [30,31][2] was applied into the contact mask and formed a thin contact to the polymer. Lastly, the copper tape (3M, 1181) was used as the positive electrode and was pressed against the carbon powder. Devices were illuminated through the TiO_2 side using a solar lamp (AM1.5) and current–voltage measurements were taken on a Keithley model 196 digital multimeter. Measurements were taken at the University Center of Excellence for Photovoltaics Research and Education (UCEP) in the Georgia Tech School of Electrical Engineering.

2.4. Thin film characterization

All AFM measurements were performed using a Multimode™ NanoScope IIIa Scanning Probe Microscope (Veeco Metrology). The "J" piezo scanner was calibrated in *x*, *y*, and *z* using NIST-certified calibration gratings (MikroMasch). Microlever™ AFM probes (Part #MLCT-AUHW, Veeco Metrology) possessing spring constants of approximately 0.03 N/m were used for most imaging conditions. For moisture-sensitive samples, a custom-built nitrogen sleeve enclosed the AFM and was held at a relative humidity of less than 10%. All contact mode AFM images were obtained under the minimal load required (setpoint) to maintain contact with the substrate. All images were composed of 512 data points per line at 512 lines per image. Tracking of the torsional movement of the cantilever (friction mapping) was also done to interpret the degree of surface coverage of all chemical layers used in creating the solar cell. This mode of data collection can discriminate between hydrophilic and hydrophobic regions of a substrate at the sub-micron level. In some instances, it was necessary to image samples utilizing Tapping Mode™ AFM. In these instances, cantilevers possessing resonant frequencies around 280 kHz were used (Model CSC 12, MikroMasch).

All roughness values reported herein are AFM based root mean square (RMS) roughness values using the standard equation

$$R_q = \sqrt{\frac{\sum (Z_i - Z_{ave})^2}{N-1}}$$

[2] The issue of obtaining anhydrous charcoal and mechanisms of sorption of water by charcoal has been discussed in the literature, e.g. studies by Puri et al. [30], later refined by Phillips et al. [31]. The moral of their findings was not only that removal of water was important for obtaining and maintaining dehydrated charcoal, but also removal of oxygen and oxygen-containing gasses like CO and CO_2, which serve as nucleation sites for water, is crucial. Complete water desorption requires elevated temperatures, with those usually used in the above-cited papers at temperature is 175 °C or higher. In our experiments, we have used charcoal that had been dried at 110 °C and kept at that temperature prior to use. In our previous experience no difference in cell performance was observed if we used charcoal dried at 110 °C or 450 °C as long as it was kept in a desiccator.

where Z_i is the z height of the ith pixel, Z_{ave} is the average of all z heights in a single image and N is the number of pixels. AFM topographical images were acquired at 10 different, non-overlapping domains on the surface. The RMS roughness for each image was determined following a first-order plane fit.

Samples for scanning electron microscopy (SEM) analysis were prepared by placing small amounts of Aquadag colloidal graphite (Ted Pella) onto standard aluminum specimen mounts (Ted Pella) and then immobilizing the sample of interest on the colloidal graphite. Since some of the samples were moisture sensitive, following immobilization, the samples were stored overnight under a nitrogen atmosphere. All samples were analyzed using a S-800 SEM (Hitachi) equipped with energy-dispersive X-ray (EDX) microanalysis (Thermo Kevex X-ray, Model 3600-0398). All spectroscopic measurements were made using a driving voltage of 7–9 kV.

A SSX-100 X-ray photoelectron spectrometer (Surface Science Laboratories Inc.) with an Al Kα X-ray source (1486.6 eV) was used for angle-resolved XPS studies. The base pressure was around 6.7×10^{-9} Pa. Film thicknesses were measured using a Tencor Alpha-Step 500 profilometer. Optical micrographs were obtained with an Olympus BX51 microscope operated in reflectance mode.

3. Results and discussion

3.1. TiO_2 electrode characterization

The CTO glass and TiO_2 electrodes were characterized using AFM, SEM–EDX, XPS, and optical microscopy to determine the effect of the morphology of the underlying substrate upon subsequential layer depositions as well as on the overall device performance. Kapton tape was used to mask the CTO underlayer from sol–gel deposition. The adhesive of the tape was chemically resistant to the solvents used in these experiments. Application of the sol–gel through spin-coating at 17, 25, 33 and 50 rps produced 100, 70, 40, and 12 nm thick films, respectively. The tape, however, is not a perfect mask. At the rotation speeds used, the sol–gel seeps under portions of the tape leaving an irregular interface. As a result, film thickness had to be measured using profilometry rather than AFM. Optical microscopic images obtained after sintering of the TiO_2 film deposited at spin speeds of 17 rps (Fig. 1a) and 33 rps (Fig. 1b) reveal significant differences in surface morphologies. The thicker film (Fig. 1a) is highly fractured during the sintering process whereas the thinner film (Fig. 1b) is uniform.

Two concerns with using Kapton tape as a mask are: (1) removal of the tape may leave behind an adhesive residue and (2) the adhesive (or its removal) modifies the surface morphology of the underlayer. To alleviate these concerns, native fluorinated tin oxide glass was half-covered with Kapton tape and then removed. Ten contact mode images were acquired at randomly chosen locations on the unmasked portion of the slide. The average RMS roughness for the fluorinated tin oxide glass was 10.3 ± 1.1 nm. The tape was removed from the masked portion and 10 additional contact mode images were acquired. The average RMS roughness for the tape-treated surface of the fluorinated tin oxide was 10.8 ± 1.4 nm. This value is statistically equivalent to that found for the unmasked side. This result leads us to conclude that the tape adhesive does not modify the surface morphology of the CTO surface. Force curves were also acquired at various positions on the surface of both the masked and unmasked portions of the CTO surface. Equivalent rupture forces were obtained. This finding supports the hypothesis that no tape residue was left behind by the Kapton adhesive.

Next, a native fluorinated tin oxide glass substrate with Kapton tape covering half of the glass was treated and spun at 17 rps with a low viscosity sol–gel. Contact mode AFM and friction mapping were carried out to determine the average surface roughness and the degree of coverage (Fig. 2). The average RMS roughness of this film was 9.1 ± 0.5 nm. It is important to note that the friction map (Fig. 2b) demonstrates that the cantilever experiences a high amount of torque. This can be attributed to the high degree of hydrophilicity of the TiO_2 [10] as well as the thicker film having a higher degree of residual solvent present. On the other hand, if a high viscosity sol–gel was deposited at 17 rps and sintered for over 1 h at 450 °C, we observe a drastically different looking surface. First, the film itself fractures (as depicted optically in Fig. 1). It was of interest to determine whether the film had

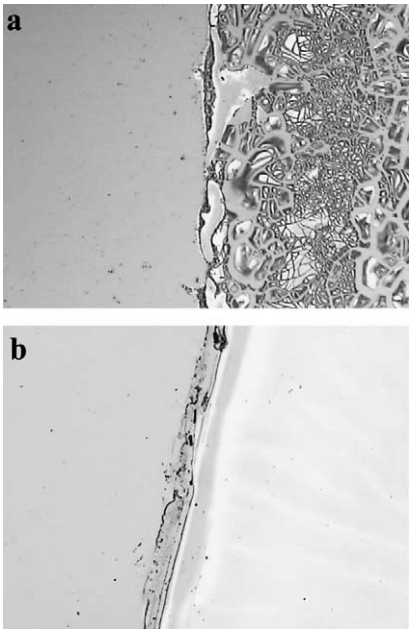

Fig. 1. Optical micrographs depicting the interface between SnO_2:F and the TiO_2 thin film spin-cast at (a) 17 rps, and (b) 33 rps. The images were acquired after sintering at 450 °C for 30 min. As seen in these photographs, the severe cracking observed in (a) was caused from the thickness of the TiO_2 layer under a considerable amount of stress, whereas the thinner TiO_2 layer shown in (b) does not crack under the same sintering conditions.

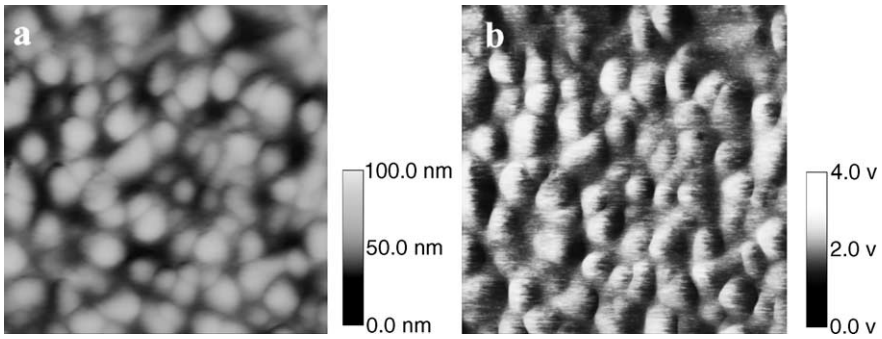

Fig. 2. Contact mode AFM image of the surface of a TiO_2 thin film obtained from a low viscosity TiO_2 sol–gel spun at 17 rps and sintered at 450 °C for 30 min. (a) Topographical image of a 1 μm × 1 μm domain and (b) friction map of the same region.

totally fractured or had simply blistered at the surface of the film. SEM was used to characterize the bulk morphology of the fractured film in parallel, EDX spectroscopy was used to determine elemental composition of the film. Fig. 3 presents a SEM image of a highly fractured TiO_2 film. Close inspection of the image reveals that each of the fractured parts of the film were still under a considerable amount of stress. This is based on the observation that the middle of each TiO_2 fragment contains a darker region, which most likely represents the portion of the TiO_2 that remains in contact with the native glass. EDX spectra of the cracked TiO_2 (Fig. 4a) confirmed that the fracturing led to the exposure of the underlying SnO_2:F substrate (Fig. 4b). This explains why solar cell devices fabricated from films prepared in this manner always failed. Next, using AFM we investigated the surface morphology of the individual islands composing this fractured film. Circular voids were found in the islands that ranged from 150 to 400 nm in diameter (Fig. 5a). These voids could have potentially been generated during the out-gassing of the solvent in the sol–gel. It was also found that the areas between these nanometer-sized voids possess surface morphologies that were significantly different (Fig. 5b) than the morphology of the unstressed film that was cast under optimal conditions (Fig. 2b). The morphology that was observed in Fig. 5b was a highly crystalline lattice that has an average RMS roughness of 0.42 ± 0.22 nm. Others have observed the enhancement of all PV solar cell parameters with an increase in sintering temperature, best results obtained for TiO_2 electrodes sintered at 450 °C for 12 h [32].

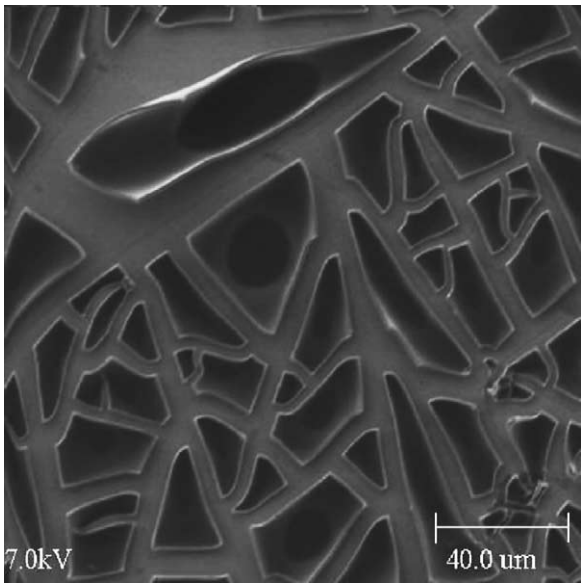

Fig. 3. SEM image of high viscosity sol–gel TiO_2 spun at 17 rps and sintered for over 1 h at 450 °C. We have concluded that these "islands" of TiO_2 are also stressed and only attached to the underlying glass at the dark regions located near the center of each TiO_2 fragment.

Solvent-cast TiO_2 that was spun at 33 rps yielded slightly smoother and uniform films (RMS roughness = 7.9 ± 0.8 nm) (Fig. 6a). The friction map illustrates that a uniform torque is induced on the cantilever (Fig. 6b). The friction map also demonstrates another interesting point: the cantilever is torqued less when probing this film as opposed to the TiO_2 that was cast at 17 rps. A potential explanation for this could be that since the 17 rps film is thicker, it can absorb a higher amount of water than the thinner (33 rps) film.

Reduction of the sintering time to 30 min produced uniform, flat TiO_2 films without cracking for films with thicknesses less than 70 nm (Fig. 1b). High resolution XPS data shown in Fig. 7 matched those previously reported for anatase TiO_2 [26]. Best device performances (55.0 μA/cm^2, V = 0.693 V) were found with 40 nm TiO_2 films sintered for 30 min; therefore, a defect-free TiO_2 layer acted as an efficient blocking layer. Current–voltage curves acquired with cells made by these procedures have already been published [33]. Additionally, performance versus time measurements have been reported on cells produced in the same manner which have shown that current and voltage measurements improved over time [33].

3.2. Polymer layer characterization

Sintered TiO_2 films removed from the furnace at 120 °C were quickly placed in a P3UBT-chloroform solution to pro-

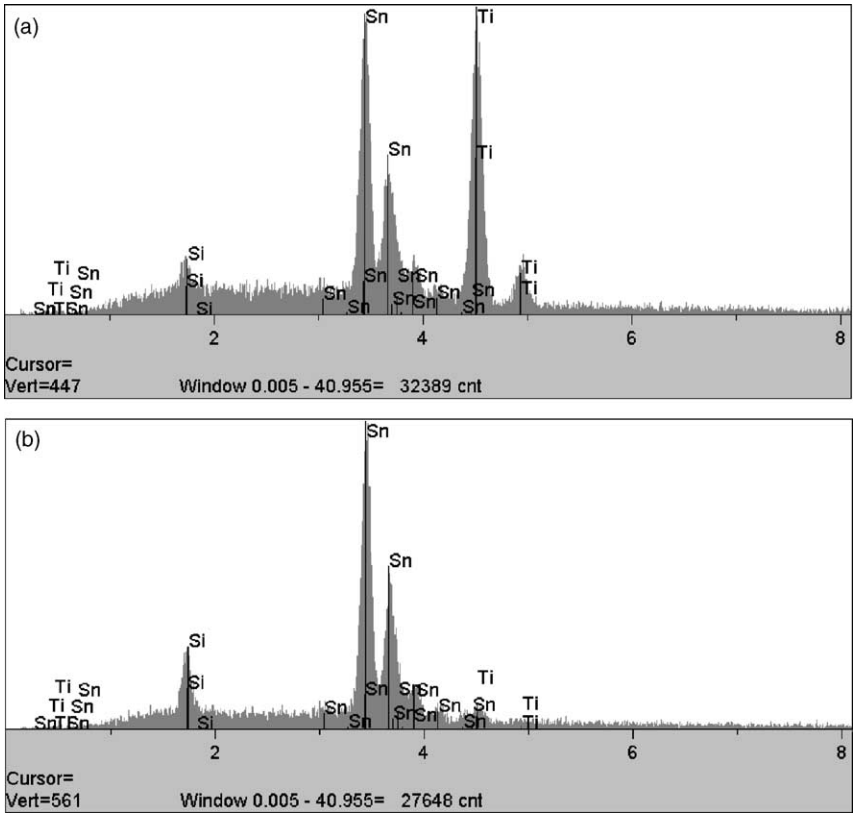

Fig. 4. EDX spectra of a high viscosity TiO_2 sol–gel spun at 17 rps and sintered for over 1 h at 450 °C. Spectrum (a) was acquired on a TiO_2 island whereas spectrum (b) was acquired between TiO_2 islands.

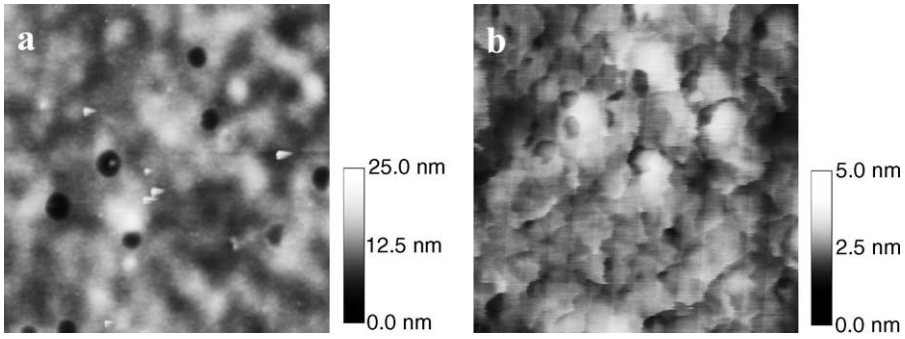

Fig. 5. Tapping Mode™ AFM images of crystalline TiO_2 islands. (a) A 6 μm × 6 μm micrograph that demonstrates the presence of nanoscale pits in the TiO_2 islands and (b) 300 nm × 300 nm micrograph of the smooth area between the circular pits.

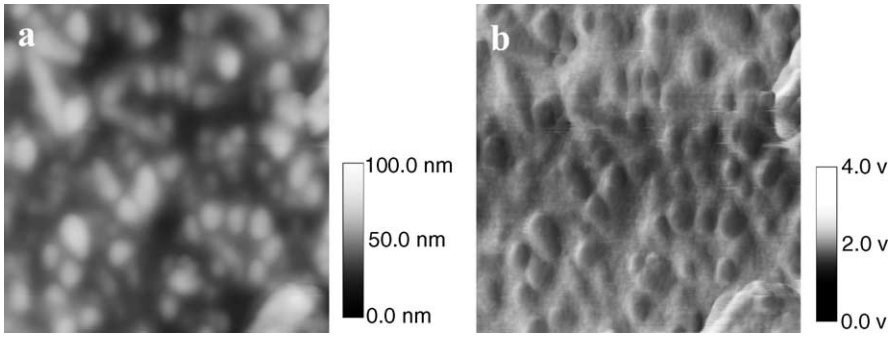

Fig. 6. AFM images of spin-cast sol–gel TiO_2 spun at 33 rps and sintered for 30 min. (a) Topographical and (b) friction images of the same 1 μm × 1 μm domain.

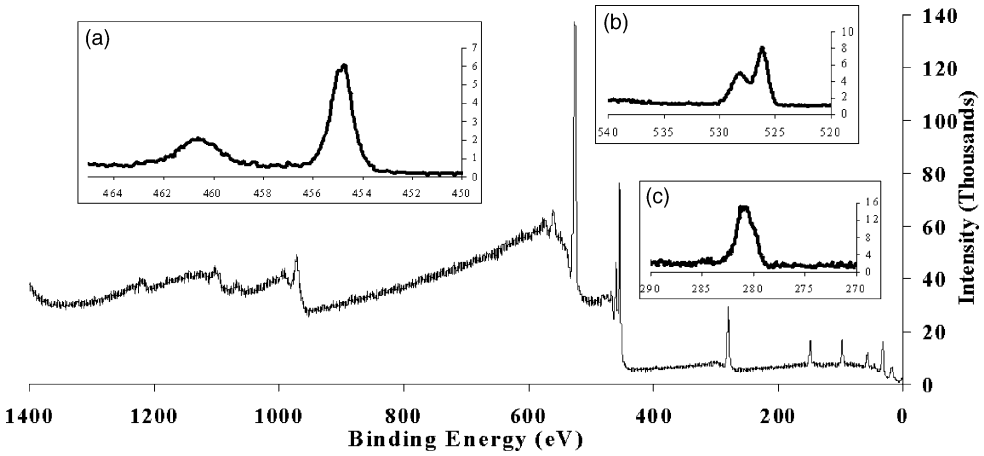

Fig. 7. XPS survey scan of TiO_2 including insets: (a) high resolution Ti-2p, (b) high resolution O-1s and (c) high resolution C-1s.

tect the TiO_2 by preventing water absorption onto the film. Devices constructed without protecting the TiO_2 layer failed to produce measurable current or voltage. Sintered TiO_2 films were rapidly placed into heated solutions containing either 0.4 mg/ml or 4.0 mg/ml P3UBT in chloroform in order to protect the TiO_2 while absorbing the polythiophene into the nanoporous surface. Although the thin P3UBT films absorbed onto the TiO_2 surface were of the desired thickness, they contained polymer aggregates measuring several microns in diameter as seen in the optical microscopy pictures in Fig. 8.

Next, it was necessary to characterize the surface morphology of the P3UBT adsorbed layer. Initially we found that this layer possessed particles that were embedded in the film (Fig. 9a). AFM topological measurements of the areas between the aggregates (Fig. 9b) yielded an average RMS roughness of 6.70 ± 0.65 nm. Devices fabricated from polymer films that exhibited these aggregate structures yielded working devices of low efficiencies ($2.0\,\mu A/cm^2$, $V = 0.25 \pm 0.05$ V). It is postulated that these aggregates could be penetrating to the TiO_2 layer, creating a short in the final solar cell device.

Due to the formation of these large aggregates, the P3UBT-chloroform protecting solution was not used to prevent moisture absorption by the TiO_2. Instead, dried chloroform was used as the protecting solvent, while solutions of warm 0.4 and 4.0 mg/ml P3UBT-chloroform were spin-cast at speeds between 17 and 50 rps. It was found that speeds less than 33 rps resulted in films similar to those described for the absorption layers. However, spin speeds of 33 rps or greater led to uniform, aggregate-free films able to protect the hydrophilic TiO_2 layer. When uniform spin-cast P3UBT films were achieved, AFM surface analysis yielded an average RMS roughness of 5.26 ± 0.45 nm (Fig. 10a) and coating of samples was extremely uniform as depicted by the friction image (Fig. 10b).

P3UBT cast layers were prepared as described in Section 2. UV-Vis of the polythiophene cast layer exhibited an absorbance of 0.33 ± 0.02 at $\lambda_{max} = 525$ nm, while the underlying spin-cast layers displayed an absorbance of only 0.04 at the same wavelength. The data confirms that of previous reports for the P3UBT [10]. It was apparent from this data that the PV device has a sufficient light absorption ability to produce mA/cm^2 of photocurrent, yet only $\mu A/cm^2$

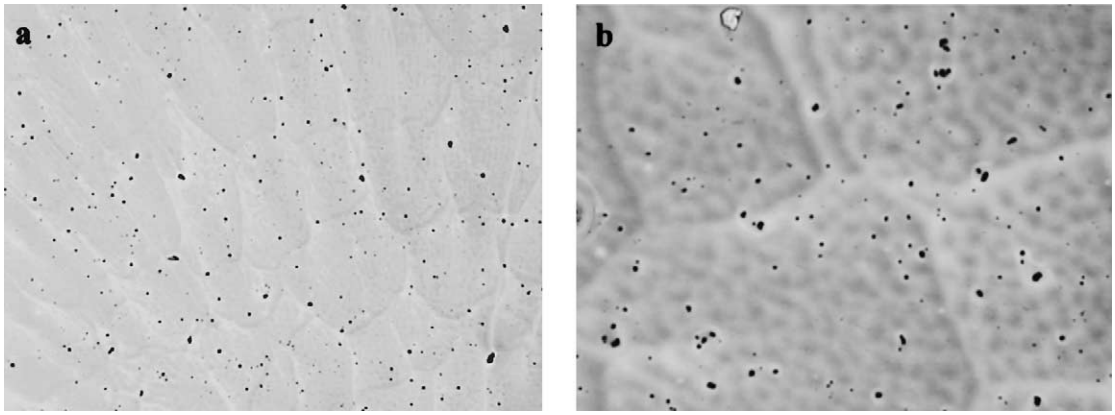

Fig. 8. Optical microscopy of P3UBT film containing aggregates. (a) 5 times normal magnification (b) 20 times normal magnification.

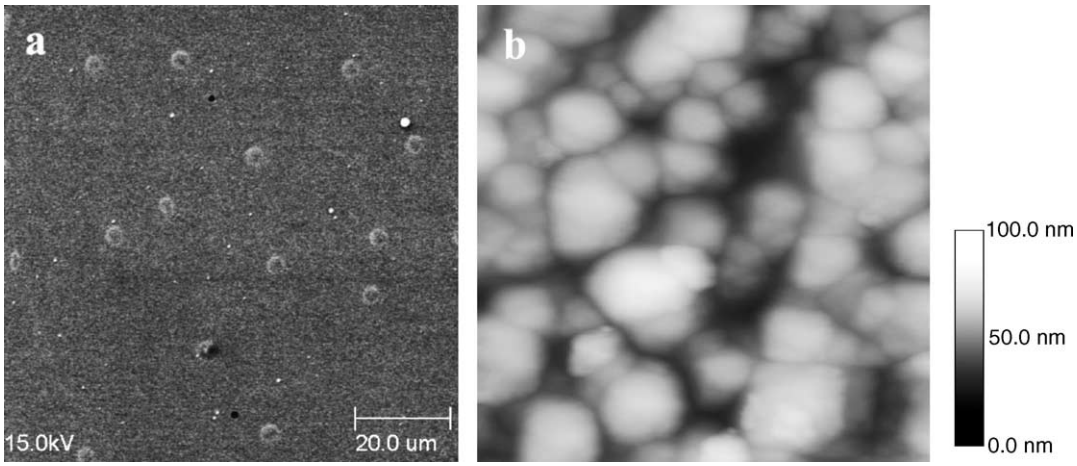

Fig. 9. (a) SEM image of the P3UBT spin-cast layer spun at 17 rps and (b) Tapping Mode™ AFM topographic image of the area between the aggregates (1 μm × 1 μm).

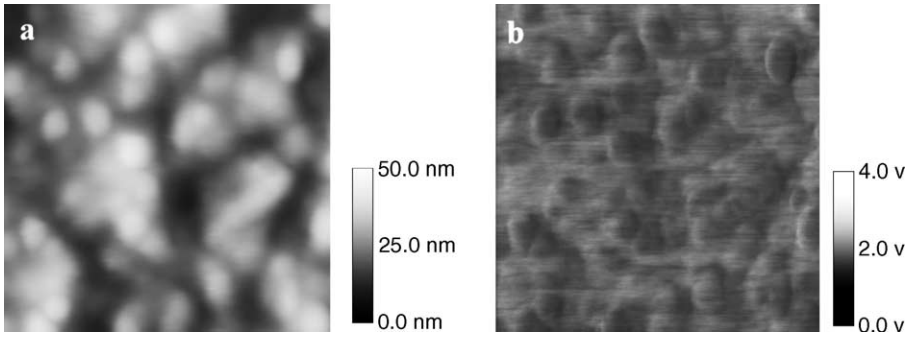

Fig. 10. AFM Image of a uniform spin-cast P3UBT film. (a) 1 μm × 1 μm topographical image and (b) corresponding friction map. (*Note:* There is less frictional contrast than either of the TiO_2 layers.)

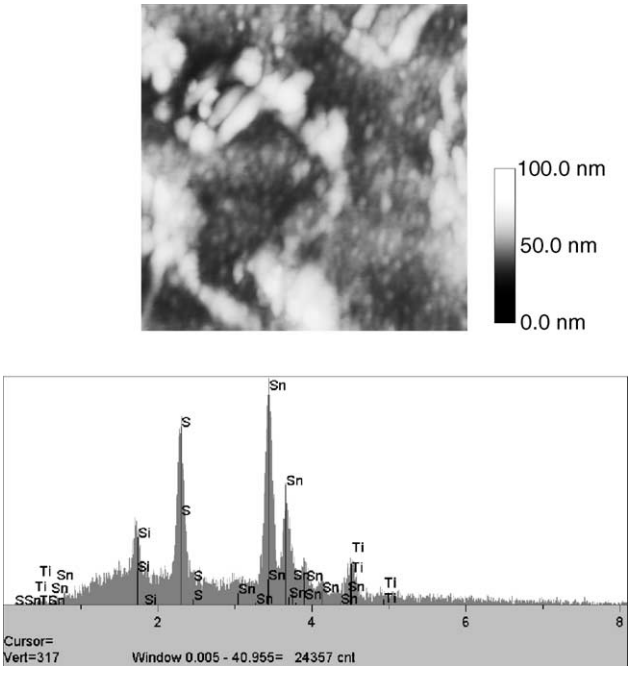

Fig. 11. (a) 2 μm × 2 μm Tapping Mode™ AFM image of a typical solvent-cast P3UBT layer and (b) EDX spectrum of the cast layer.

were observed in the previous studies [1,33,34]. The most likely explanation for this is that only a monolayer or two of polymers coordinated at the TiO_2 interface is efficient for electron injection into the TiO_2 [34]. The absorbance from the TiO_2 film applied on SnO_2:F electrode was 0.01 at $\lambda_{max} = 450$ nm and negligible at longer wavelengths.

The solvent-cast PU3BT layer was characterized with both AFM and EDX. The topological features in the final cast layer (Fig. 11a) had smooth areas that had RMS roughnesses below 3 nm but also possessed areas that were slightly more corrugated and possessed roughnesses of approximately 7 nm. The EDX spectra that were acquired on this final polymer layer (Fig. 11b) showed a strong sulfur signature which is indicative of the P3UBT layer. PV devices designed from the combination of the best P3UBT and TiO_2 layers resulted in devices that facilitated maximum light absorption by the polymer to create flat solid-state photovoltaic cells with $J_{sc} = 55\ \mu A/cm^2$ and $V_{oc} = 0.7$ V.

4. Summary, conclusions, and future work

It has been demonstrated that the morphological properties of each layer in an inorganic–organic hybrid solar

device strongly influences the overall efficiency of the photovoltaic cell. Each additional layer exhibits a planarizing effect which can only enhance the contact of subsequent layers. Fracture planes and inhomogeneties in the TiO_2 and aggregates in the P3UBT layers lead to PV devices of low efficiency or a total destruction of the electrical output of the PV cell. Surface morphologies can be determined rapidly and easily, although only qualitatively, through optical microscopy in reflection mode at 5–20 times magnification, while for quantitative analyses, SEM–EDX and AFM need to be employed. There is still much room left for optimizing the sol–gel and polymer coating processes by systematically and narrowly changing the parameters, such as solution viscosity, spin rate, and sintering process.

More research is currently being carried out to further elucidate the mechanism(s) that limit the efficiency and electrical output of inorganic–organic hybrid solid-state PV solar cell devices. We have previously explored functionalizing polythiophenes with phosphonate end-groups to achieve better intimate contact between TiO_2 and the polymer [33], while others have recently explored the effect of carboxyl-functionalized polythiophenes in PV devices [35,36]. The functionalized end-groups have led to an improvement in the performance of inorganic–organic hybrid solar cells; therefore, studying the surface morphologies created through the use of such functionalizations has become the focus of our future work.

Acknowledgements

This paper is dedicated to Michael Grätzel of the EPFL who was the inspiration for this study and all of our studies relating to DSSCs. We thank Yolande Berta of the Electron Microscopy Center at Georgia Tech for helpful discussions regarding the SEM work, Jiri Janata for granting access to his optical microscope and spin coaters, Ajeet Rohatgi for use of his solar cell testing equipment, and Ebony Mays for assistance in interpreting the XPS data. This work was made possible by a research grant from the Department of Energy. M.A. Poggi would like to thank NASA Langley for partial support of this project through funding from the GSRP program.

References

[1] C.D. Grant, A.M. Schwartzberg, G.P. Smestad, J. Kowalik, L.M. Tolbert, J.Z. Zhang, J. Electroanal. Chem. 522 (2002) 40.
[2] D.M. Chapin, C.S. Fuller, G.L. Pearson, J. Appl. Phys. 25 (1954) 676.
[3] A. Rohatgi, J.-W. Jeong, Appl. Phys. Lett. 82 (2003) 224.
[4] S. Narasimha, A. Rohatgi, in: Proceedings of the 26th IEEE PV Specialists Conference, 1997, p. 63.
[5] M.A. Poggi, L.A. Bottomley, P.T. Lillehei, Anal. Chem. 74 (2002) 2851.
[6] M. Gomez, J. Rodriguez, S. Tingry, A. Hagfeldt, S.E. Lindquist, C.G. Granqvist, Sol. Energy Mater. Sol. Cells 59 (1999) 277.
[7] J. Kocka, A. Fejfar, H. Stuchlikova, J. Stuchlik, P. Fojtik, T. Mates, B. Rezek, K. Luterova, V. Svrcek, I. Pelant, Sol. Energy Mater. Sol. Cells 78 (2003) 493.
[8] J.P. Bearinger, C.A. Orme, J.L. Gilbert, Surf. Sci. 491 (2001) 370.
[9] N. Stevens, C.I. Priest, R. Sedev, J. Ralston, Langmuir 19 (2003) 3272.
[10] L. Sirghi, T. Aoki, Y. Hatanaka, Surf. Rev. Lett. 10 (2003) 345.
[11] Y. Leprince-Wang, K. Yu-Zhang, Surf. Coat. Technol. 140 (2001) 155.
[12] D. Franta, I. Ohlidal, P. Klapetek, P. Pokorny, Surf. Interface Anal. 34 (2002) 759.
[13] M. Zaharescu, M. Crisan, I.J. Musevic, Sol–Gel Sci. Technol. 13 (1998) 769.
[14] N.J. Cherepy, G.P. Smestad, M. Graetzel, J.Z. Zhang, J. Phys. Chem. B 101 (1997) 9342.
[15] I.N. Hulea, R.F.J. Van Der Scheer, H.B. Brom, B.M.W. Langeveld-Voss, A. Van Dijken, K. Brunner, Appl. Phys. Lett. 83 (2003) 1246.
[16] S.J. Martin, A. Kambili, A.B. Walker, Phys. Rev. B: Cond. Mater. Mater. Phys. 67 (2003) 165214/1.
[17] V. Lemaur, E. Hennebicq, J. Cornil, D. Beljonne, J.L. Bredas, Chimie Nouvelle 21 (2003) 73.
[18] M.K. Nazeeruddin, A. Kay, I. Rodicio, R. Humphry-Baker, E. Mueller, P. Liska, N. Vlachopoulos, M. Graetzel, J. Am. Chem. Soc. 115 (1993) 6382.
[19] E. Palomares, J.N. Clifford, S.A. Haque, T. Lutz, J.R. Durrant, J. Am. Chem. Soc. 125 (2003) 475.
[20] B. O'Regan, M. Graetzel, Nature (London) 353 (1991) 737.
[21] M. Grätzel, Nature (London) 414 (2001) 338.
[22] E. Stathatos, P. Lianos, S.M. Zakeeruddin, P. Liska, M. Graetzel, Chem. Mater. 15 (2003) 1825.
[23] P. Wang, S.M. Zakeeruddin, P. Comte, I. Exnar, M. Graetzel, J. Am. Chem. Soc. 125 (2003) 1166.
[24] G.P. Smestad, Sol. Energy Mater. Sol. Cells 76 (2003) 1.
[25] S. Spiekermann, G. Smestad, J. Kowalik, L.M. Tolbert, M. Grätzel, Synth. Met. 121 (2001) 1603.
[26] H. Liu, W. Yang, Y. Ma, Y. Cao, J. Yao, J. Zhang, T. Hu, Langmuir 19 (2003) 3001.
[27] C.J. Barbe, F. Arendse, P. Comte, M. Jirousek, F. Lenzmann, V. Shklover, M. Grätzel, J. Am. Ceram. Soc. 80 (1997) 3157.
[28] S. Narayan, P. Desai, A.S. Abhiraman, J. Kowalik, L. Tolbert, in: AnTech. Conf.-SPE 56th, 1998, p. 1317.
[29] J. Kowalik, L.M. Tolbert, S. Narayan, A.S. Abhiraman, Macromolecules 34 (2001) 5471.
[30] B.R. Puri, K. Murari, D.D. Singh, J. Phys. Chem. 65 (1961) 37.
[31] J. Phillips, D. Kelly, L. Radovic, F. Xie, J. Phys. Chem. B 104 (2000) 8170.
[32] Y.-Q. Wang, S.-G. Chen, X.-H. Tang, O. Palchik, A. Zaban, Y. Koltypin, A.J. Gedanken, Mater. Chem. 11 (2001) 521.
[33] C.D. Grant, A.M. Schwartzberg, G.P. Smestad, J. Kowalik, L.M. Tolbert, J. Zhang, Z. Synth. Met. 132 (2003) 197.
[34] G.P. Smestad, S. Spiekermann, J. Kowalik, C.D. Grant, A.M. Schwartzberg, J. Zhang, L.M. Tolbert, E. Moons, Sol. Energy Mater. Sol. Cells 76 (2003) 85.
[35] Y.-G. Kim, J. Walker, L.A. Samuelson, J. Kumar, Nano Lett. 3 (2003) 523.
[36] G.K.R. Senadeera, K. Nakamura, T. Kitamura, Y. Wada, S. Yanagida, Appl. Phys. Lett. 83 (2003) 5470.